Electrochimica Acta 215 (2016) 637–646

Contents lists available at ScienceDirect

Electrochimica Acta

journal homepage: www.elsevier.com/locate/electacta

La/Ba-based cobaltites as IT-SOFC cathodes: a discussion about the effect of crystal structure and microstructure on the O_2-reduction reaction

Diana Garcés[a], Analia L. Soldati[b], Horacio Troiani[b], Alejandra Montenegro-Hernández[b], Alberto Caneiro[b], Liliana V. Mogni[b,*]

[a] Centro Atómico Constituyentes, Av. Gral Paz 1499, Buenos Aires, Argentina
[b] CONICET-CNEA, Centro Atómico Bariloche, Av. Bustillo 9500, S.C. Bariloche, CP 8400, Argentina

ARTICLE INFO

Article history:
Received 6 May 2016
Received in revised form 23 August 2016
Accepted 28 August 2016
Available online 31 August 2016

Keywords:
IT-SOFC
perovskite
cathode
O2-reduction reaction
LBC

ABSTRACT

This work discusses the effect of the crystal structure and microstructure on the electrocatalytic activity of Lanthanum-Barium cobaltite (LBC), evaluatedas IT-SOFC cathode. Two systems with similar microstructures (particle sizes $d_p \approx 1–5\ \mu m$) are used to compare the effect of the crystal structure: the cubic $La_{0.5}Ba_{0.5}CoO_{3-\delta}$ with La/Ba cations randomly distributed, and a tetragonal $LaBaCo_2O_{6-\delta}$ with La/Ba layered distribution. In addition, the effect of microstructure is studied by using a newsol-gel route which allows obtaining $LaBaCo_2O_{6-\delta}$ with smallest particle size ($d_p \approx 500$ nm). The electrode reaction isstudied by electrochemical impedance spectroscopy (EIS) as a function of temperature (T) and oxygen partial pressure (pO_2). The electrode polarization resistance ($R_{C,P}$) presents two contributions, a low frequency (R_{LF}) and a high frequency Gerischer-resistance (R_G). On one side, R_{LF}, associated to the O_2-gas diffusion across the gas layer boundary, presents low activation energy (E_a) and is proportional to pO_2^{-1}, presenting the same values regardless the microstructure.On the other side, R_G is in agreement with anO_2-reduction mechanismco-limited by O-surface exchange and O-bulk diffusion. R_G is strongly influenced by structure (trough the diffusion coefficient D_V) and microstructure (inversely proportional to d_p). Besides, R_G decreases by reducing d_p and by modifying the La/Ba ordering from layered to randomly distributed.

1. Introduction

The Solid Oxide Fuel Cells (SOFCs) are promising devices designed to improve efficiency and to develop a cleaner energy generation [1,2]. These cells can produce electricity when they are feeded with hydrocarbons or bio combustibles, can produce renewable fuels (H_2, CO) by reverse work in the electrolysis mode [3,4] and also can store electricity by switching between the fuel cell and the electrolysis modes [5]. Despite the good perspectives of this technology, the irruption of these devices in the market is limited by the high costs of production and operation and degradation issues, mainly due to the high working temperatures (T > 800 °C) which limit the span of operation life. Thus, recent research efforts have been focused on finding new materials able to operate with better performances in an intermediate temperature range (500–700 °C, IT-SOFC) [6].

Regarding the device performance, the highest loss of efficiency of an IT-SOFC is originated in the cathode side, due to the high activation energy of the O_2 electrode reaction [7]. Two complementary strategies can be adopted to reduce the cathode polarization resistance ($R_{C,P}$): first, the use of new oxides with mixed ionic and electronic conductivity (MIEC) increasing the reaction zone beyond the triple phase boundary, and second, the increase of the electrode's specific surface by adopting nanostructured materials.

Cobaltites with perovskite structure, and mainly the Strontium-Barium cobaltites (BSCF) [8,9], are one of the most promising cathode materials for IT-SOFCs. In these perovskites, the Ba plays a key role since its large cation radii distorts the cubic crystal structure promoting the oxygen vacancy formation and migration [10]. In addition, Ba atoms also assist the O_2 reduction kinetics and reduce the $R_{c,p}$ due to the improvement of the O-surface exchange and the O-ion diffusion. However, the same structural distortion,

* Corresponding author. Tel.: +54 294 4445288.
E-mail addresses: mogni@cab.cnea.gov.ar, lilianamogni@gmail.com (L.V. Mogni).

http://dx.doi.org/10.1016/j.electacta.2016.08.132
0013-4686/

also induces a slow segregation of an hexagonal perovskite phase [11–13], which deteriorates the O_2 reduction kinetics with time [14].

Beside the BSCF cobaltites, other Barium-based perovskites such as $La_{1-x}Ba_xCoO_{3-\delta}$(LBC) with x = 0.4-0.7 [15–18] and $La_{1-x}Ba_xCo_{1-y}Fe_yO_{3-\delta}$(LBCF) [19] also exhibit low $R_{C,P}$. As in the case of BSCF perovskites, the cubic phase is metastable below 1000 °C, affecting the long term stability [15]. In this context, the $LnBaCo_2O_{6-\delta}$ layered perovskites (Ln = La, Pr, Nd, Sm, Gd) became attractive cathode materials. These oxides not only present $R_{C,P}$ values as low as 0.02-0.5 Ωcm^2 at 700 °C (i.e $LaBaCo_2O_{6-\delta}$ [20] $PrBaCo_2O_{6-\delta}$ [21] $NdBaCo_2O_{6-\delta}$ [22–25], $SmBaCo_2O_{6-\delta}$ [26], $GdBaCo_2O_{6-\delta}$ [22,27–29]), high rates of oxygen surface exchange and O-ion diffusivity [30–34] and electrical conductivity [21,35], but also show a huge advantage over the other Ba-based cobaltites: the formation of the hexagonal phase has not been observed in the ordered tetragonal phase.

The cationic order in $LnBaCo_2O_{6-\delta}$ layered perovskites oxides takes place due to the large difference between the ionic radii of Ba^{2+} and Ln^{3+} ions. As a consequence of this, the ionic and electronic transport are affected [36]. However, it remains unclear wether the cationic ordering modifies the mechanism of the O_2-reduction reaction, decreasing the polarization resistance, or not. With the aim of answering this topic, the electrochemical response of two materials, which differ only in their crystal structure (the cubic $La_{0.5}Ba_{0.5}CoO_{3-\delta}$ and the tetragonal $LaBaCo_2O_{6-\delta}$) wasevaluated.

As mentioned above, it is well known that the cathode polarization resistance can be appreciably decreasedbyimproving theelectrode's microstructure. Indeed, the polarization resistance decreases orders of magnitude for (La,Sr)$CoO_{3-\delta}$ [37,38] (La,Sr)(Co,Fe)$O_{3-\delta}$ [39–43] and (Sm,Sr)$CoO_{3-\delta}$ [44] perovskites with particle size below 100–200 nm. Therefore, this work also explores a sol-gel route in order to obtain $LaBaCo_2O_{6-\delta}$ with two different particle sizes and evaluates the changes in theirperformancewhen working as electrodes.

2. Experimental

2.1. Synthesis

Powder samples, with nominal $La_{0.5}Ba_{0.5}CoO_{3-\delta}$, (LBC) composition were obtained by two different methods: the conventional Solid State Reaction method (SSR) and a Soft Chemical Route (SCR) involving a gel formation by polymerization of Acetyl-Acetone (AcAc) and Hexamethylenetetramine(HMTA).

The SSR method was previously used to obtain cubic $La_{0.5}Ba_{0.5}CoO_{3-\delta}$ and tetragonal $LaBaCo_2O_{6-\delta}$ from La_2O_3 (99.99%, Alfa Aesar), Co_3O_4 (99.7%, Alfa Aesar) and $BaCO_3$ (99.95%, Alfa Aesar) by applying different heat treatments under air and Ar atmospheres, respectively [36].

In this work, the SCR method was optimized to obtain both, the cubic and tetragonal phases, at mild conditions (lower temperatures and/or shorter times). In this case, the starting La_2O_3, $BaCO_3$ and $Co(CH_3COO)_2$ (99.9%, Fluka) materials were mixed in a solution of acetic acid (AcH, Cicarelli), AcAc (99.5%, Carlo Erba) and HMTA (≥99.5%, Sigma Aldrich). The relationship between organic and inorganic components, defined as C_o/C_i ($C_o = C_{HMTA} = C_{acac}$and $C_i = C_{La+3} + C_{Ba+2} + C_{Co+2}$), was fixed in 3 to 1. The AcH acts as a solvent, whereas the AcAc and HMTA are chelating agents and polymer precursors. These precursors facilitate the polycondensation and polyesterification reactions, forming a network of metal-organic polymers. The solution was heated at ~80 °C and kept under water reflux for 2 h. After that, a few drops of H_2O_2were added. Both, heat and H_2O_2 accelerate the polymerization/gelation reaction. The produced gel was heated at 450 °C for two hours and further calcinedat 750 °C during 12 h for removing organic material.

The powders obtained were treated at different temperatures and atmospheres in order to find the optimal synthesis conditions to obtain the adequated sample features (see Table 1). Once the phases were obtained, an annealing at 400 °C in air for 6 h was performed for samples synthesized under Ar atmosphere in order to ensure oxygen incorporation.

The phase purity of the synthesized powders was checked by X-ray diffraction (XRD) using a Philips PW1700 diffractometer with Cu-Kα radiation and a graphite monochromator.

2.2. Structural and Microstructural Study

LBC samples synthezed in air and Ar after the annealing at 400 °C in air for 6 h were structurally characterized by combining XRD and High-Resolution Transmission Electron Microscopy (HR-TEM). High statistic XRD patterns were collected and analyzed by the Rietveld method using Fulproof [45]. Two structural models were used: a cubic structure belonging to the *Pm* 3 *m* Space Group and a tetragonal *P*4/*mmm* [36]. These models included micro-strain effects, considerations about isotropic or anisotropic atomic relative vibrational motion, and the location and concentration of oxygen vacancy defects.

The materials were also studied by Transmission Electron Microscopy (TEM) with a Philips CM 200 UT equipment. Bright/Dark field images, HR-TEM images and Selected Area Electron Diffraction (SAED) patterns were obtained and compared to simulated patterns/HR-TEM images. Simulations were performed with the software JEMS (Java versionV3-3526U2008s, CIME-EPFL), using structural parameters obtained from the Rietveld analyses.

In addition, the microstructures were characterized by Field Emission Gun Scanning Electron Microscopy (FEG-SEM) with a FEI Nova NANO 230 microscope. This characterization was complemented with TEM to determine particle size distribution.

Table 1
Details of the heat treatment performed after the different routes of synthesis and main sample characteristics (see Section 3.1).

Type	Structure	Method	Label	Heating conditions			Sample Characteristics	
				T (°C)	time (h)	Atm.	Structure	Particle size
La/Ba radom distributed	$Pm\bar{3}m$ Cubic	Solid State Reaction	SSR-1100-Air	1100	12	Air	$a = b = c$= 3.8915(1)Å [36]	5–10 μm
		Soft Chemical Route	SCR-1100-Air	1100	2	Air	--	5–10 μm[a]
			SCR-1050-Air	1050	12	Air	--	--
La/Ba layered distributed	*P*4/*mmm* Tetragonal	Solid State Reaction	SSR-1150-Ar	1150	24	Ar	$a = b$ = 3.9147(1), c = 7.6999(1)Å [36]	5–10 μm
		Soft Chemical Route	SCR-1150-Ar	1150	2	Ar	--	5–10 μm[a]
			SCR-900-Ar	900	24	Ar	$a = b$ = 3.8942(1), c = 7.7860(4)Å	200–500 nm

[a] agglomerates of 500 nm particles.

2.3. Electrochemical Characterization

The electrode reaction was investigated by electrochemical impedance spectroscopy (EIS) on symmetrical cells. The cells consist of a dense $Ce_{0.9}Gd_{0.1}O_{1.95}$(GDC, Fuel Cell Materials surface area 34.6 cm^2/g) electrolyte (area ~0.8 cm^2, thickness ~0.1 cm), where a porous layer of GDC and a porous layer of LBC were deposited by *spin coating*. The inks were prepared by mixing the corresponding ceramic powders (GDC or LBC) with ethanol, α-terpineol (≥96%, Sigma Aldrich), polyvinyl butyral (Sigma Aldrich), and polyvinyl pyrrolidone (Sigma Aldrich) in a 40:40:27:2:1 mass ratio.The porous layer of GDC improves the adherence of LBC cathode onto the GDC dense electrolyte [16]. After deposition, the porous GDC layer was heat treated at 1350 °C during 1 h in air, while the LBC porous electrode was heat treated at the same temperature and under the same atmosphere than those used to obtain each LBC sample (see Table 1). The electrode thicknesses (~12–15 μm) were determined by SEM.

The EIS measurements were carried out in air as a function of temperature between 400 and 800 °C. EIS spectra were also collected at 500, 600 and 700 °C varying the oxygen partial pressure (pO_2) between 1 and 5×10^{-4} atm by using a home-made device to test symmetrical cells coupled to an electrochemical oxygen pump and sensor. The EIS data were collected with an Autolab-PGSTAT32 potentiostat with a FRA2 module. The frequency was varied between 1 MHz y 0.1 mHz and the signal applied consisted in a 0 V bias with 5 mV amplitude. Impedance spectra were analyzed with a Matlab code [46] using an electrical equivalent circuit.

3. Results

3.1. Synthesis and Characterization

The minimum temperature to obtain both LBC phases by the soft chemical reaction method was determined by comparison of the XRD patterns of SCR-T-Air and SCR-T-Ar (see Table 1) with those synthesized by solid state reaction (the cubic $La_{0.5}Ba_{0.5}CoO_{3-\delta}$ SSR-1100-Air and the tetragonal $LaBaCo_2O_{6-\delta}$ SSR-1150-Ar). Fig. 1 shows the resultant XRD patterns and Fig. 2 shows the FEG-SEM images of the as-synthesized powders.

The treatment in air allows to obtain a single cubic phase justat 1100 °C, independently of the synthesis route used (Fig. 1a). Indeed, three peaks of an unknown secondary phase are present at 2θ between 25 and 35 degrees for the SCR powders treated in air at T ≤ 1050 °C, which dissapear at 1100 °C. From the microstructural point of view, the particle's sizes obtained by both methods (SSR-1100-Air andSCR-1100-Air) are similar (i.e. d_p ~5–10 μm, Fig. 2), indicating that the critical parameter to obtain the cubic phase is the temperature (1100 °C) rather than the synthesis route itself.The main difference between both methods is that the SCR requieres shorter thermal treatments than the SSR in order to obtain the desired phase (see Table 1).

The synthesis temperature of the tetragonal phase can be appreciably reducedbyusing a chemical route (in this case, both samples were burned under Ar flow). In both cases, a pure phase is obtained at 1150 °C, as it is shown from the splitting of the diffraction peaks associated to the cation ordering in BaO-CoO_2-LaO-CoO_2-BaO layers (see Fig. 1b). Furthermore, none extra peaks are detected even using synthesis temperatures as low as 900 °C (Fig. 1b), although the particle sizes decrease from d_p ~5–10 μm for SSR-1150-Ar to d_p ~ 200–500 nm for SCR-900-Ar (Fig. 2b).

A secondary effect on the decrease of the heat treatment temperature is that the splitted peaks of the micrometric sized sample merged to broad peaks in the nanometric sample, and it becomes difficult to discern if they correspond to a tetragonal, a cubic or a mix of both phases.To solve this issue, high statistic X-ray diffraction patterns were collected for SCR-900-Ar samples in order to obtain structural data by using the Rietveld method. The structural models applied were based in a combination of XRD and neutron diffraction data, for cubic and tetragonal phase, respectively [36]. As it was mentioned before, the diffraction pattern of SCR-900-Ar does not clearly show whether the sample presents acubic, a tetragonal or a mixture of both symetries. Then, these three possibilities were tested, including the presence of microstrain associated to each symmetry [47]. The goodness-of-fit, χ^2, decreases from 7.36 to 6.67 and 5.85 as the proposed symmetry changes from "cubic" to a mix of "cubic + tetragonal" and a pure "tetragonal" phase. The measured and the calculated diffraction profiles are included in the supplementary information (Fig. S1), the estimated structural parameters are shown in Table 1.

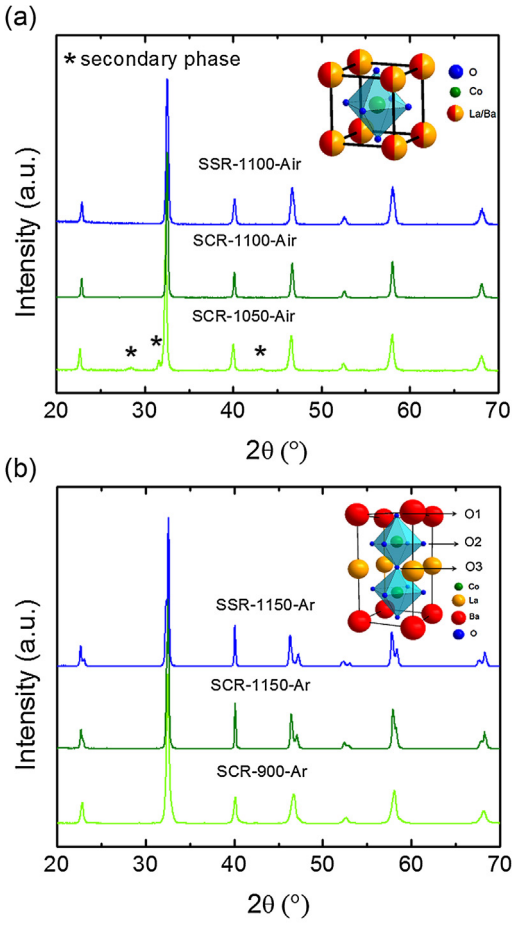

Fig. 1. XRD patterns of LBC. (a) synthesized in air SSR-1100-Air, SCR-1100-Air and SCR-1050-Air. (b) synthesized in Ar SSR-1150-Ar, SCR-1150-Ar and SCR-900-Ar.

HRTEM images with their FFT diffractograms and simulated electron diffraction patterns complemented the structural analysis. Fig. 3a.*i*, b.*i* and c.*i* show the HR-TEM for the SCR-1100-Air, SCR-1150-Ar and SCR-900-Ar, respectively. The FFT's (ii) of the HR-TEM images were compared with akinematic simulation of the diffraction patterns (iii). These simulations were based on published structural data for cubic $La_{0.5}Ba_{0.5}CoO_{3-\delta}$and tetragonal $LaBaCo_2O_{6-\delta}$ [36], and from the refinement of XRD pattern of SCR-900-Ar sample.

First, the SAED simulated pattern of SCR-1100-Air (shown in Fig. 3a.*iii*) is in agreement with the FFT diffraction pattern obtained along the $[113]_C$ zone axis (ZA) for acubic *Pm* 3 *m* structure. Second, the electron diffraction pattern of SCR-1150-Ar and SCR-900-Ar (shown in Fig. 3b.*iii* and c.*iii*) match with those simulated along the

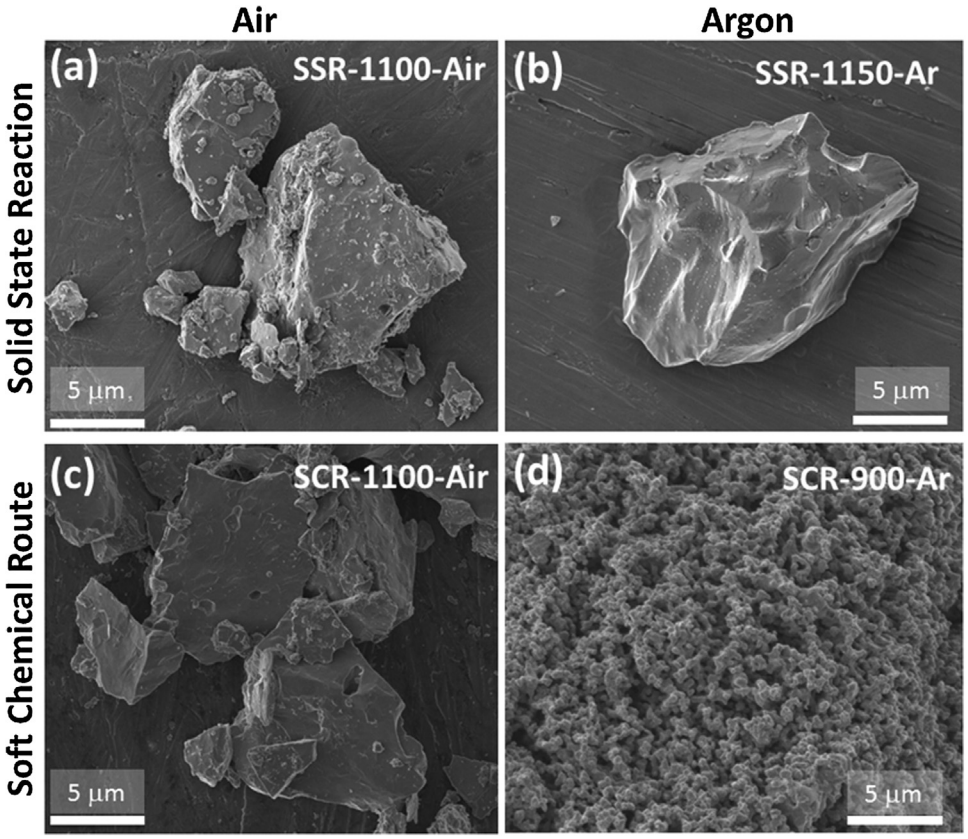

Fig. 2. FEG-SEM images of the as-synthesized powders a) SSR-1100-Air, b) SSR-1150-Ar, c) SCR-1100-Air and d) SCR-900-Ar.

$[201]_T$ and $[110]_T$ ZA for atetragonal *P4/mmm* symmetry.These results confirm the cationic order structure suggested by the Rietveld refinement for the SCR-900-Ar.

The TEM analyses also produces complementary information to that obtained by SEM about the particle size and morphology. Crystallite-size distributions were achieved from statistical measurements by using bright/dark field images (Fig. 4). Regarding the particles morphology, SCR-900-Ar shows more rounded forms with a narrow particle size distribution, while both samples synthetized at higher temperatures show a wide particle size distribution with the presence of micrometer grains (which is in agreement with the SEM pictures shown at Fig. 2). In these cases, a normal distribution model is no longer supported, and therefore the median and the mode are also reported in the histograms. At higher temperatures, but under the same reductive atmosphere (i.e. comparing SCR-900-Ar versus SCR-1150-Ar) the average crystallite size remains around 500 nm, but the median diminishes. This is probably due to the formation of aggregates of smaller particles (see Fig. 2). By changing the atmosphere to air (i.e. comparing SCR-1100-Air and SCR-1150-Ar), the particles grain size median and mode remain very similar, indicating that no big effect on the microstructure is induced.

At this point it can be concluded, from the structural analysis performed by combining electron and X-ray diffraction and from the microstructural study done by SEM and TEM, that the SCR allows obtaining a cation ordered phase with tetragonal structure and particle size below 500 nm.These results are not possible to obtain with SSR method.

3.2. Electrode characterization

The $R_{C,P}$ was determined by EIS measurements on symmetrical cells, as a function of T and pO_2. The spectra were collected between 500 and 750 °C in air and at 500, 600 and 700 °C by varing pO_2 between 1 and 10^{-4} atm. The Nyquist and Bode plots of the EIS spectra for three samples,were included as supplementary information (Fig. S2 and S3). Table 2 compares the $R_{C,P}$ at 600 and 700 °C obtained in this work with data of some relevant perovskites type cathode(References included at Table 2). The chemical composition, crystal structure and microstructural features of each cathode are also included. The polarization resistance for the cathodes studied hereare competitive with other IT-SOFC cathode materials. Mainly, the layered $LaBaCo_2O_{6-\delta}$ synthetized by the soft chemical route, which reaches $R_{C,P}$ value as low as 0.115 and 0.055 Ωcm^2 at 600 and 700 °C, respectively.

From the Nyquist and Bode plots it can be observed that the cathodes synthetized by solid state reaction show one EIS arc, which splits into two arcs at high temperature and low pO_2. On one hand, the cathode obtained by soft chemical reaction shows two arcs, that are present in almost all conditions. Considering this, the EIS spectra were fitted by using the Electrical Equivalent Circuits (EEC) approximation, assuming a Gerischer-type (Z_G) dependence for the high frequency contribution, in series with a parallel resistor/capacitor (Z_{LF}) element for the low frequency contribution (see EEC at Table 3). It is worth to mention that the EEC was completed by adding in series an ohmic resistance and an inductancein order to take into account the electrolyte resistance and the inductance of the wires. Some examples of the fitting for EIS spectra collected at T = 700 °C and pO_2 = 0.19 atm and $pO_2 = 3 \times 10^{-3}$atm were also included as supplementary information (Fig. S4).

The $R_{C,P}$ presents two terms: R_G (real part of Z_G) and R_{LF} (real part of Z_{LF}). Fig. 5 shows the log-log plot of $R_{C,P}$, R_G and R_{LF}vs pO_2 at 500, 600 and 700 °C for all symmetrical cells. On the other hand, Fig. 6 shows the Arrhenius plot ($\ln(R_{C,P})$ vs T^{-1}) in air, which is used to obtain the activation energy (E_a) of each individual

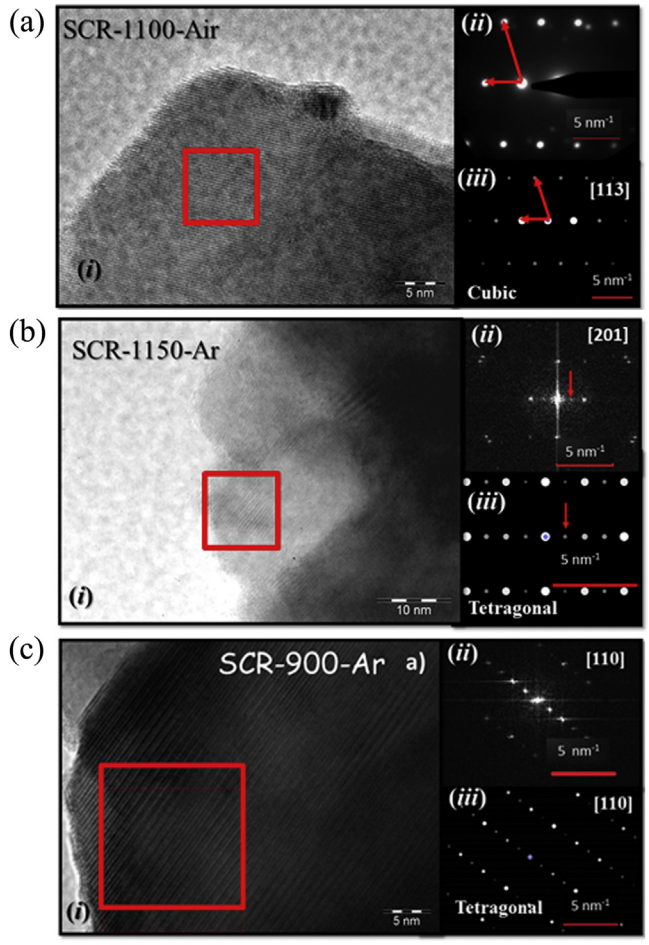

Fig. 3. HR-TEM image for (a.*i*) SCR-1100-Air, (b.*i*) SCR-1150-Ar and (c.*i*) SCR-900-Ar. Comparison between FFT of the selected area shown at HR-TEM images (a.*ii*, b.*ii* and c.*iii*) and kinematical simulation for SAED pattern along the (a.*iii*) $[113]_C$, (b.*iii*) $[201]_T$ and (c.*iii*) $[110]_T$ ZA's.

contributions. The relevant fitting parameters are resumed in Table 3. The main contribution to $R_{C,P}$ is R_G, whereas R_{LF} becomes dominant at high temperature (600 and 700 °C) and low pO_2.

The R_{LF} only seems to be a relevant polarization loss for the SCR-900-Ar sample, once the fine microstructure allows reducing the high frequency contribution to comparable values to those of R_G. Besides, this low frequency contribution is almost independent of the temperature (see Fig. 6) and strongly dependent of the pO_2 ($R_{LF} \propto pO_2^{-1}$) (see Fig. 5). Table 3 and Figs. 5 and 6 show that, in those cases where this contribution is relevant, Z_{LF} shows high capacitance values and takes almost the same values for all cells, independently of the electrode microstructure. Therefore, this low frequencies impedance arc is associated to the concentration polarization loss due to the O_2-gas diffusion, not only inside the pores but also trough the layer boundary between the porous electrode and the gas phase.

It can be assumed that the electrode polarization loss due to the activation process is Z_G. For the three cathodes, Z_G is described by a Gerischer-type impedance:

$$Z_G = R_G \frac{1}{\sqrt{1 + j\omega\tau_G}} \quad (1)$$

where $j = \sqrt{-1}$, and R_G and τ_G are the Gerischer resistance and time constant, respectively. This type of impedance element was used by Adler-Lane-Steel at the ALS model to describe the impedance response of porous single-phase MIEC oxides, where the O_2-reduction rate was co-limited by the O-surface exchange and diffusion processes [48,49]. The pseudo-capacitance can be calculated as $C_G = \tau_G/R_G$ [48]. Table 3 indicates the pO_2 dependence, the activation energy and the minimum and maximum values of R_G and C_G at 700 °C and different pO_2. Both, the resistance and the pseudo-capacitance for all electrodes increase as pO_2 decreases. The cubic perovskite shows the largest C_G values, which increases with T reaching values above 1 Fcm^{-2} at 800 °C. Contrary, for both layered perovskites, C_G decreases from 0.15 to 10^{-2} Fcm^{-2} as T increases.The resistance R_G depends on the structural (or intrinsic material's properties) and microstructural features trough:

$$R_G = \frac{RT}{4F^2} \frac{1}{\sqrt{4a\Re_O c_O x_V^0 (1+2\nu) D_{V,ef}}} \quad (2)$$

In this equation, the molar equilibrium oxygen surface exchange rate ($\Re o$), the effective O-diffusion coefficient ($D_{V,ef} = \frac{(1-\varepsilon)D_V}{\tau_s}$), the concentration of oxygen sites (c_O) and the molar fraction of O-vacancy at equilibrium (x_V^0) constitute intrinsic properties of the material. Alternatively the electrode porosity (ε), the electrode specific surface area (a) and the MIEC-phase tortuosity factor (τ_s) are volume-averaged microstructural features. (F is the Faraday constant and R is the universal gas constant). The R_G can be considered as the geometric mean between the O-diffusion (R_D) and O-surface(R_S) resistances: $R_G = \sqrt{R_D R_S}$.

The parameter ν is a dimensional coefficient taking into account the possibility of a parallel O-surface diffusion path [49]:

$$\nu = \frac{surface O - diffusion}{bulk O - diffusion} = \frac{\Gamma_o \theta_{O_s}^0 D_{O_s}}{R c_O x_V^0 D_V} \quad (3)$$

The effect of the parallel O-surface path was illustrated in ref [49]. The authors studied two La-Sr cobaltites, the O-diffusion coefficient of $La_{0.6}Sr_{0.4}CoO_{3-\delta}$ is independent with pO_2 because the O-bulk path dominates the diffusion, whereas for $La_{0.8}Sr_{0.2}CoO_{3-\delta}$ the mechanism is dominated by O-surface diffusion and the diffusion coefficient is strongly dependent with pO_2 (trough $\theta_{O_s}^0$). In the case of the La-Ba cobaltites the high D_V obtained by O-permeation flux [30] together with high O-vacancies concentrations [36] allows assume a $\nu \sim 0$ and O-diffusion trough a bulk path.

4. Discussion

4.1. The ALS model and its range of validtiy

The ALS model has been recently used to describe the response of porous MIEC electrodes based on LSC [49], LSCF [50] and LSF [51] perovskites and NNO Ruddlesden-Popper phases [52]. In those cases where the O-diffusion follows a bulk transport path, D_V is weakly pO_2-dependent and if the O-surface exchange is controlled by the dissociative adsorption of O_2, then $\Re o \propto k_O pO_2^{0.5}$ ($k_O$is the O-surface exchange coefficient). The ALS model works well under those conditions where surface exchange and bulk diffusion have comparable resistances and time constants, and consequently co-limit the O_2 reduction. However, besides the different pO_2 dependence, k_O and D_V also show an Arrhenius dependence with T and have different activation energies. Therefore, the change between a main O-surface exchange or O-diffusion control regime can be observed depending on the experimental conditions. This effect can be illustrated by comparison of the utilization length ($l_\delta = \sqrt{\frac{D_{V,ef} c_O x_V^0}{4a\Re_O}}$ [48,49]) with the particle size d_p and the electrode thickness L. l_δ indicates the useful electrode thickness and depends

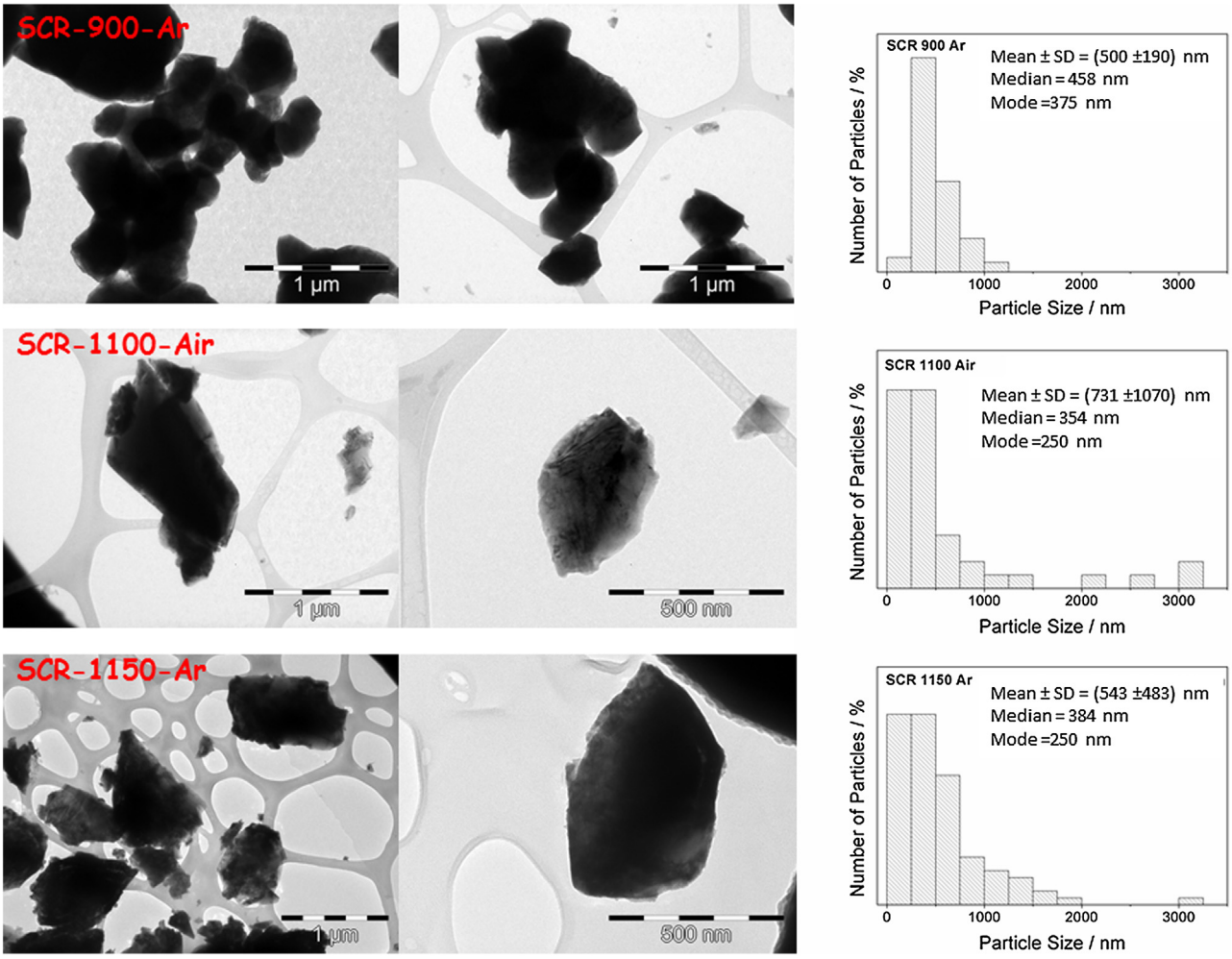

Fig. 4. Bright Field TEM images of samples SCR-900-Ar, SCR-1100-Air and SCR-1150-Ar showing the typical particle size distribution (right column).

on the intrinsic material properties (i.e. D_V, $\Re_O$) and microstructure characteristics such as the specific surface a ($a \approx d_p^{-1}$). Therefore, the utilization length becomes narrow or wide depending on the relative values of kinetic parameters and how these are affected by T and pO_2 [53] and for the same material (with the same intrinsic properties) the utilization length depends with the particle size as $l_\delta = \sqrt{d_p}$.

The ALS model is valid for $d_p << l_\delta << L$ Otherwise, if $d_p \gtrsim l_\delta$ the regime changes to an O-bulk diffusion controlled regime, which can eventually confine the reaction to the triple phase boundary (TPB) electrode/electrolyte/gas. In this case, the impedance is better represented by a Warburg-type element [54]. In those cases where $l_\delta \approx L$ the surface process became more dominated and the EIS response can be modeled by a Finite-Length-Gerischer [55]:

$$Z_{FLG} = R_G \sqrt{\frac{1}{1+j\omega t_G}} \coth\left(\frac{L}{l_\delta}\sqrt{1+j\omega t_G}\right) \quad (4)$$

This FLG equation extend the concept of a co-limit process of O-ion diffusion and O-surface exchange to a more general situation where the electrode thickness is below the utilization length ($L < l_\delta$). Note that in the limit of a thick electrode $l_\delta \ll L$, the $\coth\left(\frac{L}{l_\delta}\sqrt{1+j\omega t_G}\right) \approx 1$ and the ALS model is recovered, whereas if $l_\delta >> L$ the $\coth\left(\frac{L}{l_\delta}\sqrt{1+j\omega t_G}\right) \approx \left(\frac{L}{l_\delta}\sqrt{1+j\omega t_G}\right)^{-1}$ and the impedance transforms to a R//Cpe-type element. Fig. 7 shows different situations where microstructure, the relative values of O-diffusion (R_D) and O-surface (R_S) resistances, can produce a change of regime regarding the validity of the ALS model.

In this work, it was found the same pO_2-dependence for R_G ($R_G \propto pO_2^{-0.25}$)independently of temperature, La/Ba cationic order or disorder, or the cathode microstructure (Fig. 6, solid lines). This dependence is in agreement with a $D_V$independent of pO_2 and a $\Re o \propto k_O pO_2^{0.5}$, as in other porous cathodes where the ALS model was applied. The same pO_2 dependence was also reported for LSCF electrodes, $La_{0.8}Sr_{0.2}Co_{0.2}Fe_{0.8}O_{3-\delta}$ [56] and $La_{0.6}Sr_{0.4}Co_{0.2}Fe_{0.8}O_{3-\delta}$ [57]. However, in those cases, the authors attributed this dependence to a mechanism controlled by a surface process in agreement with a low pseudo-capacitance values ranging between $\sim 10^{-3}$ to 0.15 Fcm^{-2}. Amin et al. [17] analyzed the EIS response as a function of T and pO_2 of a porous $La_{0.5}Ba_{0.5}CoO_{3-\delta}$ (LBC) electrodes in terms of EEC based on two constant phase elements (R//CPEs) in series. They found similar pO_2 dependence and activation energy than in this work. They assumed that the high frequency response is due to oxygen ion transport followed by charge transfer at the electrolyte/electrode interface.

In this work, the capacitance of the Gerischer impedance(C_G) of the LBC electrodes take values around 10^{-2}-1 Fcm^{-2}(See Table 3), increasing its values as pO_2 decreases. These high values of pseudo-capacitances are are in agreement with a mechanism involving a significant bulk contribution [58]. The lower surface control for O_2-reduction in LBC electrodes compared with LSCF could be explained by the high surface activity reported for these La-Ba

Table 2
Comparison of the characteristic cathode polarization resistances for single phase porous electrodes in air.

	Composition		≈ d_p(μm)	$R_{C,P}$ (Ωcm^2) 600 °C	700 °C	Ref.
La/Ba randomly distributed with Cubic *Pm-3 m* (C) or Orthorhombic−*Pbnm* (O)	$La_{0.5}Ba_{0.5}CoO_{3-\delta}$	C	5-10	0.35	0.15	this work
		C	1	0.16	0.09	[17]
		C	0.5	0.12	0.035	[18]
	$La_{0.4}Ba_{0.6}CoO_{3-\delta}$	C	5-10	0.14	0.04	[16]
	$La_{0.3}Ba_{0.7}Co_{0.6}Fe_{0.4}O_{3-\delta}$	C	5-10	0.6	0.12	[19]
	$Ba_{0.5}Sr_{0.5}Co_{0.8}Fe_{0.2}O_{3-\delta}$	C	--	0.07	--	[9]
		C	--	0.09	0.022	[64]
	$Ba_{0.5}Sr_{0.5}Co_{0.2}Fe_{0.8}O_{3-\delta}$	C	1-5	0.61	0.17	[65]
	$La_{0.6}Sr_{0.4}CoO_{3-\delta}$	--	0.017	0.023	--	[38]
		--	0.5-1	3.77	0.657	[66]
	$Sm_{0.5}Sr_{0.5}CoO_{3-\delta}$	--	0.5	2.5	--	[67]
		--	0.2	0.2	0.035	[44]
		O	0.2	0.12	0.03	[68]
	$La_{0.4}Sr_{0.6}Co_{0.8}Fe_{0.2}O_{3-\delta}$	C	0.685	1.5	0.3	[39]
		C	0.045	0.07	0.04	
		C	0.130	0.05	0.03	[40]
	$La_{0.6}Sr_{0.4}Co_{0.2}Fe_{0.8}O_{3-\delta}$	--	0.1-0.5	6.23	0.82	[50]
		--	0.5	3	0.3	[20]
La/Ba layered distributed with Tetragonal *P4/mmm* (T) or Orthorhombic -*Pmmm* (O)	$LaBaCo_2O_{6-\delta}$	T	5-10	1.5	0.6	This work
		T	0.5	0.115	0.055	This work
		O	0.5-1	3.5	0.5	[21]
		T	0.5-1	--	0.06	[20]
	$PrBaCo_2O_{6-\delta}$	O	0.5-1	0.213	0.025	[21]
		O	--	0.7	0.15	[22]
		O	0.5-1	0.4	0.08	[23]
		T	1	0.87	0.18	[69]
	$NdBaCo_2O_{6-\delta}$	O	0.5-1	0.3	0.035	[21]
		T	--	0.4	0.067	[22]
		T	1-2	1.1	0.11	[24]
		O	--	0.67	0.08	[25]
	$SmBaCo_2O_{6-\delta}$	O	0.5-1	0.5	0.08	[21]
		O	1-2	0.56	0.12	[26]
	$GdBaCo_2O_{6-\delta}$	O	0.5-1	0.25	0.035	[21]
		O	--	0.21	0.15	[22]
		O	--	1	0.3	[27]
		O	1-2	0.4	0.08	[28]
		--	5	1.11	0.27	[29]

Table 3
Relevant electrochemical data obtained from the fitting of the electrochemical impedance spectra with the electrical equivalent circuit (EEC) as a function of T and pO_2.

Sample			$R_{C,P}$		EEC(*) reference values at 700 °C, between pO_2 ≈1 and −10^{-4}atm					
Label	Structure	d_P (μm)	R (Ω cm^2) (700 °C, air)	E_a (eV)	Z_G (high frequency range) $R_G \propto pO_2^{-1.25}$			Z_{LF} (low frequency range) $R_{LF} \propto pO_2^{-1}$		
					R_G (Ω cm^2)	C_G (Fcm^{-2})	E_a (eV)	R_{LF} (Ω cm^2)	C_{LF} (Fcm^{-2})	E_a (eV)
SSR-1100-Air	Cubic	5-10	0.1-0.15	0.93(2)	0.11/1.3	0.05/0.8	0.99(2)	--/10	1	0.4(1)
SSR-1150-Ar	Tetragonal	5-10	0.3-0.6	1.01(3)	0.5/5.6	0.01/0.5	1.01(3)	--/5	1	--
SCR-900-Ar	Tetragonal	0.5	0.035-0.045	0.96(4)	0.025/0.082	0.03/0.16	1.17(3)	--/7	1-3	0.0(1)

(*)EEC: 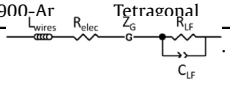

cobaltites [59]. The O-bulk diffusion is also supported by the activation energies E_a of the Gerischer impedance. These E_a reach values around 1 eV for all LBC electrodes, which are below those reported by Amin et al. (1.47 eV) for ionic conductivity in blocking electrodes [17]. Nevertheless these values are comparable to that extracted from the Arrhenius plot of the oxygen permeation flux (jO_2) in dense membranes of $La_{0.5}Ba_{0.5}CoO_{3-\delta}$ (1.1-1.2 eV)[30]. Note that the activation energy values in the Gerischer resistance (∼1 eV) are high compared with the activation energies for O-diffusion and O-surface exchange reported for other Barium based perovskites. For example, Tsai et al. [60] reported E_a ∼ 0.64-0.75 eV for O-ion flux on dense membranes of $La_{1-x}Ba_xFe_{0.8}Co_{0.2}O_{3-\delta}$ perovskites, whereas Taskin et al. [33] obtained E_a = 0.67 eV for O-Diffusion and E_a = 0.81 eV for O-surface exchange in $GdBaCo_2O_{6-\delta}$ layered perovskites. The general trend for Lanthanide-Barium layered perovskites is that E_a (O-surface exchange) >E_a (O-bulk diffusion) [61].

4.1.1. Crystal structure influence

In order to determine the influence of the crystal structure on the electrode response, a comparison between samples SSR-1100-Air and SSR-1150-Ar was performed. The R_G's ratio between this two samples was computed. These samples present similar microstructures (i.e. same ε, a and τ_s values), but different crystal structures, therefore it was assumed that c_O and x_V^0 change proportionally. Besides, the molar equilibrium oxygen surface exchange rate can be derived for different rate-limiting mechanism [62] and for those cases where the O2 exchange is limited by

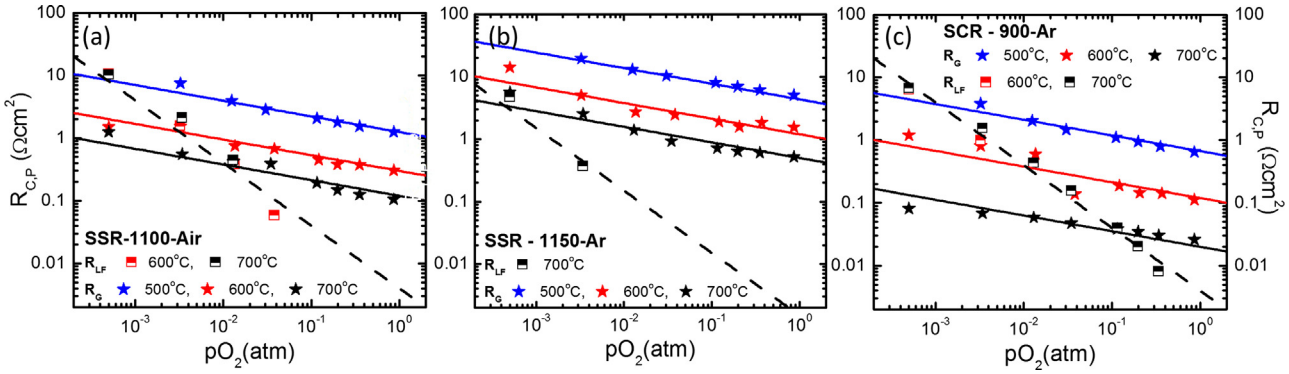

Fig. 5. Log-log graphics for the high frequency Gerischer resistance (R_G) and the low frequency resistance (R_{LF}) with pO_2 at 500, 600 and 700 °C. (a) SSR-1100-Air, (b) SSR-1150-Ar and (c) SCR-900-Ar samples. Solid lines indicate the fitting of the pO_2 dependence: $R_G \propto (pO_2)^{-0.25}$ and $R_{LF} \propto (pO_2)^{-1}$.

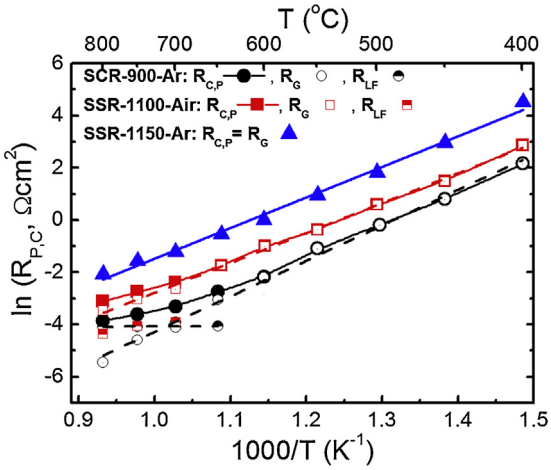

Fig. 6. Arrhenius plot for the overall cathode polarization resistance $R_{C,P} = R_G + R_{LF}$ (filled symbols), and its contributions R_G (open symbols) and R_{LF} (half and half symbols). The activation energies (E_a) for each contribution are present at Table 3.

dissociative adsorption, the exchange rate scaled as $\Re o \propto k_O pO_2^{0.5} x_V^0$ [49,52]. Then, from Eq. (2):

$$\left(\frac{R_G^{SSR_t}}{R_G^{SSR_c}}\right)^2 \approx \frac{k_O^c D_V^c}{k_O^t D_V^t} \tag{5}$$

where "SSR_c" refers to cubic symmetry (SSR-1100-Air) and "SSR_t" to the tetragonal one (SSR-1150-Ar). De Souza et al. [63] found a correlation between the O-surface exchange coefficient and the O-diffusion coefficient: $k_O \propto D_V^n$, with n ≈ 0.5-1 for electron-carrier-rich mixed conductors and n ≈ 3-4 for poor electron-carrier materials. The lanthanum-barium cobaltites belong to the first class so it can be estimated the following correlation:

$$\left(\frac{R_G^{SSR_t}}{R_G^{SSR_c}}\right)^2 \approx \left(\frac{D_V^c}{D_V^t}\right)^{n+1} \tag{6}$$

Fig. 8a and b show the "R_G ratio"(in this case $\left(\frac{R_G^{SSR_t}}{R_G^{SSR_c}}\right)^2$) as a function of T and pO_2, respectively. It can be noted that the "R_G ratio" between the tetragonal and the cubic phase is independent of temperature and pO_2 conditions, remaining almost constant at ~20. These results are reasonable, considering that the O-bulk diffusion must be higher for the cubic phase due to symmetry considerations (i.e. higher dimensionality). Furthermore, the fact that the "R_G ratio" is independent of T and pO_2 suggests that the activation energies for the O_2-reduction reaction (O-surface exchange+ O-diffusion) are almost the same for both samples and that both samples can be described by the ALS model in the whole range of studied experimental conditions.

4.1.2. Microstructure influence

Similarly, the effect of the microstructure among samples with identical crystal symmetry was analyzed comparing SCR-900-Ar ($d_p \approx 500$ nm) with SSR-1150-Ar ($d_p \approx 5$–10 μm). By using Eq. (2) and assuming the same intrinsic properties independently of the microstructure, the "R_G ratio" can be re-written as:

$$\left(\frac{R_G^{SCR_t}}{R_G^{SSR_t}}\right)^2 \approx \frac{\left(\frac{a(1-\varepsilon)}{\tau_s}\right)^{SSR_t}}{\left(\frac{a(1-\varepsilon)}{\tau_s}\right)^{SCR_t}} \tag{7}$$

Where "SCR_t" refers to tetragonal samples synthetized by the soft chemical route and "SSR_t" to that obtained by solid state reaction. It can be assumed that the major difference is mainly due to the specific surface (a) and that porosity (usually $\varepsilon \approx 0.4$-0.6) and tortuosity (usually $\tau_s \approx 1.1 - 1.3$) take almost the same values. In addition, the specific surface can be scaled with a particle characteristic length (i.e. the particle diameter $a \approx d_p^{-1}$), thus Eq. (7) can be reduced to:

$$\left(\frac{R_G^{SCR_t}}{R_G^{SSR_t}}\right)^2 \approx \frac{d_p^{SCR_t}}{d_p^{SSR_t}} \tag{8}$$

The "R_G ratio" between SCR-900-Ar and SSR-1100-Ar samples $\left(\left(\frac{R_G^{SCR_t}}{R_G^{SSR_t}}\right)^2\right)$ showed in Fig. 8a and b, takes values between 0.001 and 0.05. These values are in agreement with the difference between the characteristic particle size obtained by the chemical route ($d_p \approx 500$ nm) and by solid state reaction ($d_p \approx 5$–10 μm).

5. Conclusions

The effect of the crystal structure and microstructure on the electrode polarization resistance was studied for samples with the same chemical composition. LBC materials were selected as systems of study, because cationic ordered or disordered phases with different crystal structures and microstructures can be obtained by slightly modification on the synthesis routes. Thus, two comparisons were performed:

•

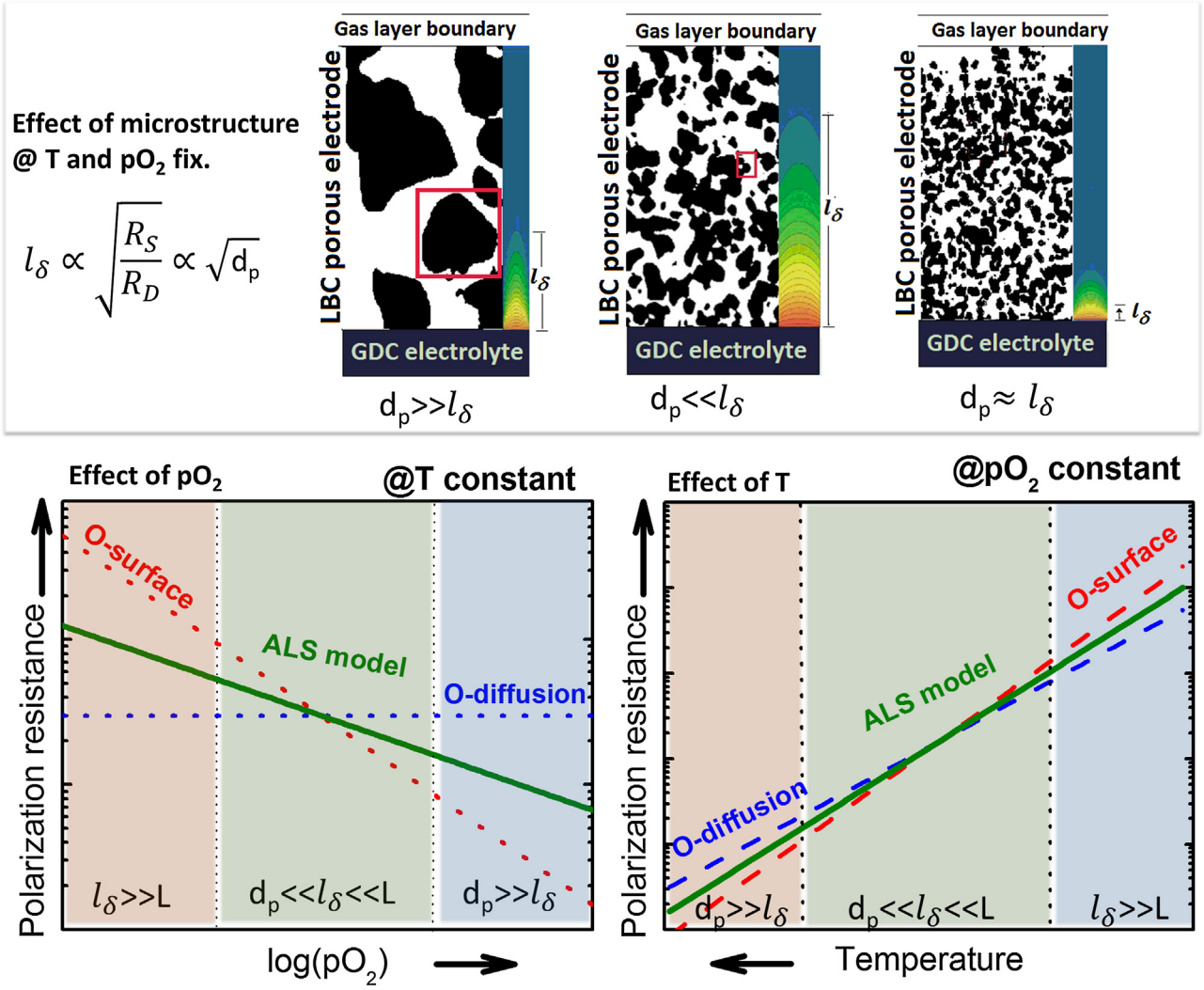

Fig. 7. Scheme of the effect of microstructure, T and pO_2 on the O_2-reduction mechanism: As the utilization length $l_\delta$decreases it became comparable to the particle size d_p and the O_2-reduction is confined to the TPB zone and controlled by the O-bulk diffusion. Red lines represent the polarization resistance due to O-surface exchange ($R_S \propto \boldsymbol{k}_O^{-1}$), blue lines those related to O-bulk diffusion ($R_D \propto \boldsymbol{D}_V^{-1}$) and green lines a co-limited resistance ($R_G = \sqrt{\boldsymbol{R}_D \boldsymbol{R}_S} \propto (\boldsymbol{D}_V \boldsymbol{k}_O)^{-0.5}$). It was assumed$E_a(O-\text{bulk diffusion}) < E_a(O-\text{surface exchange})$ [49,61].

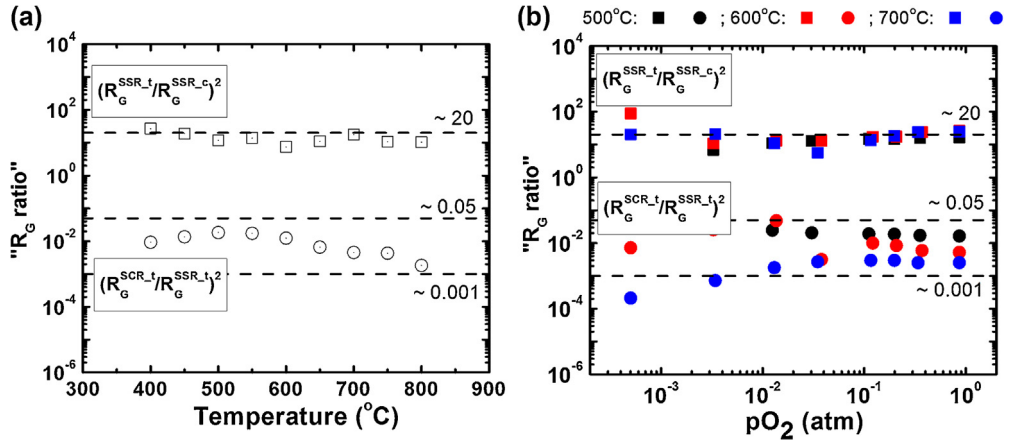

Fig. 8. "R_G ratio" (defined in the text), as a function of (a) temperature and (b) pO_2.The dashed lines indicate the "R_G ratio" estimated between the tetragonal and cubic electrodes with similar microstructure (~20) and between the tetragonal electrodes with different microstructures (~0.001-0.05).

$La_{0.5}Ba_{0.5}CoO_{3-\delta}$, vs $LaBaCo_2O_{6-\delta}$, which exhibit similar microstructures ($d_p \sim 5–10\ \mu m$) but different crystal structures ($Pm\bar{3}m$ cubic or $P4/mmm$ tetragonal space groups).
- Two $LaBaCo_2O_{6-\delta}$ with the same crystalline structure ($P4/mmm$ tetragonal phase with $a = b \approx 3.9$ and $c \approx 7.7$ Å) but with different microstructures (grain sizes $d_p \approx 5–10\ \mu m$ and $dp \approx 500$ nm).

The EIS spectra suggested that two processes contribute to $R_{C,P}$:

- The low frequency resistance (R_{LF}). This is associated to O_2 gas diffusion. R_{LF} presents a significant contribution to the polarization loss only for the electrode with the smaller particle size. The O_2 gas transport limitation seems to be due to the gas diffusion trough the layer boundary between the porous electrode and the gas phase, since the change of microstructure did not strongly affect the absolute values of R_{LF}.
- The high frequency Gerischer-resistance (R_G). In agreement with the ALS approximation, this R_G considers that the O_2-reduction reaction is co-limited by O-surface exchange and O-bulk diffusion. This mechanism is mostly determined by the crystal structure and microstructure. Then, the R_G decreases when the symmetry changes from tetragonal to cubic and when the particle size decreases due to the use of the soft chemical route.

Finally, all cathode materials presented in this paper show competitive $R_{C,P}$ values in comparison with other IT-SOFC cathodes of literature.

Acknowledgment

This work was supported by CNEA (Argentinean National Commission of Atomic Energy), CONICET (Argentinean National Council of Scientific and Technical Research), UNCuyo (National University of Cuyo), ANPCyT (National Agency for Science and Technology Promotion).

Appendix A. Supplementary data

Supplementary data associated with this article can be found, in the online version, at http://dx.doi.org/10.1016/j.electacta.2016.08.132.

References

[1] B.C.H. Steele, A. Heinzel, Nature 414 (2001) 345–362.
[2] in:K.K.S.C. Singhal (Ed.), Elsevier, Oxford, 2003.
[3] S.H. Jensen, X. Sun, S.D. Ebbesen, R. Knibbe, M. Mogensen, Int. J. Hydrogen Energy 35 (2010) 9544–9549.
[4] M. Ni, J. Power Sources 202 (2012) 209–216.
[5] S.H. Jensen, C. Graves, M. Mogensen, C. Wendel, R. Braun, G. Hughes, Z. Gao, S.A. Barnett, Energy Environ. Sci. 8 (2015) 2471–2479.
[6] Z.M. Gao, L.V. Mogni, E.C. Miller, J.G. Railsback, S.A. Barnett, Energy Environ. Sci 9 (2016) 1602–1644.
[7] A. Weber, E. Ivers-Tiffée, J. Power Sources 127 (2004) 273–283.
[8] W. Zhou, R. Ran, Z. Shao, J. Power Sources 192 (2009) 231–246.
[9] S.M.H. Zongping Shao, Nature 431 (2004) 170–173.
[10] R. Merkle, Y.a. Mastrikov, E.a. Kotomin, M.M. Kuklja, J. Maier, J. Electrochem. Soc. 159 (2012) B219–B219.
[11] K.W. Silvie Švarcová, Julian Tolchard, Henny J.M. Bouwmeester, Tor Grande, Solid State Ionics 178 (2008) 1787–1791.
[12] D.N. Mueller, R.A. De Souza, T.E. Weirich, D. Roehrens, J. Mayer, M. Martin, Phys. Chem. Chem. Phys.: PCCP 12 (2010) 10320–10328.
[13] K. Efimov, Q. Xu, A. Feldhoff, Chem. Mater. 22 (2010) 5866–5875.
[14] S. Yakovlev, C.Y. Yoo, S. Fang, H.J.M. Bouwmeester, Appl. Phys. Lett. 96 (2010) 254101–254101.
[15] C. Setevich, L. Mogni, A. Caneiro, F. Prado, J. Electrochem. Soc. 159 (2012) B73–B80.
[16] C.F. Setevich, L.V. Mogni, A. Caneiro, F.D. Prado, Int. J. Hydrogen Energy 37 (2012) 14895–14901.
[17] R. Amin, K. Karan, J. Electrochem. Soc. 157 (2010) B285–B285.
[18] S. Pang, X. Jiang, X. Li, Q. Wang, Z. Su, Int. J. Hydrogen Energy 37 (2012) 2157–2165.
[19] C. Setevich, F. Prado, D.Z. de Florio, A. Caneiro, J. Power Sources 247 (2014) 264–272.
[20] S. Pang, X. Jiang, X. Li, Z. Su, H. Xu, Q. Xu, C. Chen, Int. J. Hydrogen Energy 37 (2012) 6836–6843.
[21] K. Zhang, L. Ge, R. Ran, Z. Shao, S. Liu, Acta Materialia 56 (2008) 4876–4889.
[22] A.C. Tomkiewicz, M. Meloni, S. McIntosh, Solid State Ionics 260 (2014) 55–59.
[23] D. Chen, R. Ran, K. Zhang, J. Wang, Z. Shao, J. Power Sources 188 (2009) 96–105.
[24] J.H. Kim, J.T.S. Irvine, Int. J. Hydrogen Energy 37 (2012) 5920–5929.
[25] H. Gu, H. Chen, L. Gao, Y. Zheng, X. Zhu, L. Guo, Int. J. Hydrogen Energy 34 (2009) 2416–2420.
[26] J.H. Kim, Y. Kim, P.A. Connor, J.T.S. Irvine, J. Bae, W. Zhou, J. Power Sources 194 (2009) 704–711.
[27] A. Tarancon, D. Marrero-Lopez, J. Pena-Martinez, J. Ruiz-Morales, P. Nunez, Solid State Ionics 179 (2008) 611–618.
[28] B. Wei, Z. Lü, D. Jia, X. Huang, Y. Zhang, W. Su, Int. J. Hydrogen Energy 35 (2010) 3775–3782.
[29] N. Li, Z. Lü, B. Wei, X. Huang, K. Chen, Y. Zhang, W. Su, J. Alloys Compd. 454 (2008) 274–279.
[30] J.H. Kim, L. Mogni, F. Prado, A. Caneiro, J.A. Alonso, A. Manthiram, J. Electrochem. Soc. 156 (2009) B1376–B1376.
[31] A. Tarancón, S.J. Skinner, R.J. Chater, F. Hernández-Ramírez, J. Kilner, J. Mater. Chem. 17 (2007) 3175–3181.
[32] G. Kim, S. Wang, A.J. Jacobson, L. Reimus, P. Brodersen, C.A. Mims, J. Mater. Chem. 17 (2007) 2500–2500.
[33] A.A. Taskin, A.N. Lavrov, Y. Ando, Prog. Solid State Chem. 35 (2007) 481–490.
[34] M.n. Burriel, J. Peña-Martínez, R.J. Chater, S. Fearn, A.V. Berenov, S.J. Skinner, J. A. Kilner, Chem. Mater. 24 (2012) 613–627.
[35] J.H. Kim, F. Prado, A. Manthiram, J. Electrochem. Soc. 155 (2008) B1023–B1028.
[36] D. Garces, C.F. Setevich, A. Caneiro, G. Cuello, L. Mogni, J. Appl. Crystallogr. 47 (2014) 325–334.
[37] L. Dieterle, P. Bockstaller, D. Gerthsen, J. Hayd, E. Ivers-Tiffée, U. Guntow, Adv. Energy Mater. 1 (2011) 249–258.
[38] J. Hayd, L. Dieterle, U. Guntow, D. Gerthsen, E. Ivers-Tiffée, J. Power Sources 196 (2011) 7263–7270.
[39] C.M. Chanquía, L. Mogni, H.E. Troiani, A. Caneiro, J. Power Sources 270 (2014) 457–467.
[40] L. Baqué, A. Caneiro, M.S. Moreno, A. Serquis, Electrochem. Commun. 10 (2008) 1905–1908.
[41] F. Deganello, V. Esposito, M. Miyayama, E. Traversa, J. Electrochem. Soc. 154 (2007) A89.
[42] D. Marrero-López, R. Romero, F. Martín, J.R. Ramos-Barrado, J. Power Sources 255 (2014) 308–317.
[43] J. Liu, A.C. Co, S. Paulson, V.I. Birss, Solid State Ionics 177 (2006) 377–387.
[44] C.-L. Chang, C.-S. Hsu, B.-H. Hwang, J. Power Sources 179 (2008) 734–738.
[45] J. Rodriguez-Carvajal, Abstracts of the Satellite Meeting on Powder Diffraction of the XV Congress of the IUCr, Toulouse, France, 1990, pp. 127.
[46] J.-L. Dellis, http://www.mathworks.com/matlabcentral/fileexchange/19460-zfit 2014.
[47] P.W. Stephens, J. Appl. Crystallogr. 32 (1999) 281–289.
[48] S.B. Adler, J.A. Lane, B.C.H. Steele, J. Electrochem. Soc. 143 (1996) 3554–3564.
[49] Y. Lu, C. Kreller, S.B. Adler, J. Electrochem. Soc. 156 (2009) B513–B513.
[50] D. Marinha, L. Dessemond, J.S. Cronin, J.R. Wilson, S.A. Barnett, E. Djurado, Chem. Mater. 23 (2011) 5340–5348.
[51] A. Leonide, B. Rüger, A. Weber, W.A. Meulenberg, E. Ivers-Tiffe'e, J. Electrochem. Soc. 157 (2010) B234–B239.
[52] K. Yakal-Kremski, L.V. Mogni, A. Montenegro-Hernandez, A. Caneiro, S.A. Barnett, J. Electrochem. Soc. 161 (2014) F1366–F1374.
[53] S.B. Adler, Solid State Ionics 111 (1998) 125–134.
[54] N. Grunbaum, L. Dessemond, J. Fouletier, F. Prado, L. Mogni, A. Caneiro, Solid State Ionics 180 (2009) 1448–1452.
[55] J. Nielsen, T. Jacobsen, M. Wandel, Electrochim. Acta 56 (2011) 7963–7974.
[56] V.C. Kournoutis, F. Tietz, S. Bebelis, Fuel Cells 9 (2009) 852–860.
[57] A. Esquirol, N.P. Brandon, J.A. Kilner, M. Mogensen, J. Electrochem. Soc. 151 (2004) A1847.
[58] S.B. Adler, Chem. Rev. 104 (2004) 4791–4843.
[59] T. Ishihara, S. Fukui, H. Nishiguchi, Y. Takita, 153 (2002) 609–613.
[60] C.-Y. Tsai, A.G. Dixon, Y.H. Ma, W.R. Moser, M.R. Pascucci, J. Am. Ceram. Soc. 81 (1998) 1437–1444.
[61] M.B. Albert Tarancon, Jose Santiso, Stephen J. Skinner, John A. Kilner, J. Mater. Chem. 20 (2010) 3799–3813.
[62] S.B. Adler, X.Y. Chen, J.R. Wilson, J. Catal. 245 (2007) 91–109.
[63] R.A.D. Souza, J.A. Kilner, Solid State Ionics 126 (1999) 153–161.
[64] W. Zhou, R. Ran, Z. Shao, W. Jin, N. Xu, J. Power Sources 182 (2008) 24–31.
[65] J. Park, J. Zou, H. Yoon, G. Kim, J.S. Chung, Int. J. Hydrogen Energy 36 (2011) 6184–6193.
[66] T. Horita, K. Yamaji, N. Sakai, H. Yokokawa, E. Ivers-tiffe, Electrochem. Acta 46 (2001) 1837–1845.
[67] W.R. Changrong Xia, Fanglin Chen, Meilin Liu, Solid State Ionics 149 (2002) 11–19.
[68] S. Yoo, T.-H. Lim, J. Shin, G. Kim, J. Power Sources 226 (2013) 1–7.
[69] J. Zou, J. Park, B. Kwak, H. Yoon, J. Chung, Solid State Ionics 206 (2012) 112–119.